



ARL-TR-7598 • FEB 2016



Aerodynamic Flow Control by Thermoacoustic Excitation from the Constituent Nanomaterials on the Platform Surface

by Bryan Glaz

Approved for public release; distribution is unlimited.

NOTICES

Disclaimers

The findings in this report are not to be construed as an official Department of the Army position unless so designated by other authorized documents.

Citation of manufacturer's or trade names does not constitute an official endorsement or approval of the use thereof.

Destroy this report when it is no longer needed. Do not return it to the originator.



Aerodynamic Flow Control by Thermoacoustic Excitation from the Constituent Nanomaterials on the Platform Surface

by Bryan Glaz
Vehicle Technology Directorate, ARL

REPORT DOCUMENTATION PAGE				Form Approved OMB No. 0704-0188	
<p>Public reporting burden for this collection of information is estimated to average 1 hour per response, including the time for reviewing instructions, searching existing data sources, gathering and maintaining the data needed, and completing and reviewing the collection information. Send comments regarding this burden estimate or any other aspect of this collection of information, including suggestions for reducing the burden, to Department of Defense, Washington Headquarters Services, Directorate for Information Operations and Reports (0704-0188), 1215 Jefferson Davis Highway, Suite 1204, Arlington, VA 22202-4302. Respondents should be aware that notwithstanding any other provision of law, no person shall be subject to any penalty for failing to comply with a collection of information if it does not display a currently valid OMB control number.</p> <p>PLEASE DO NOT RETURN YOUR FORM TO THE ABOVE ADDRESS.</p>					
1. REPORT DATE (DD-MM-YYYY) February 2016		2. REPORT TYPE Director's Research Initiative (DRI)		3. DATES COVERED (From - To) October 2012–October 2015	
4. TITLE AND SUBTITLE Aerodynamic Flow Control by Thermoacoustic Excitation from the Constituent Nanomaterials on the Platform Surface				5a. CONTRACT NUMBER	
				5b. GRANT NUMBER	
				5c. PROGRAM ELEMENT NUMBER	
6. AUTHOR(S) Bryan Glaz				5d. PROJECT NUMBER FY13DRI-008	
				5e. TASK NUMBER	
				5f. WORK UNIT NUMBER	
7. PERFORMING ORGANIZATION NAME(S) AND ADDRESS(ES) US Army Research Laboratory ATTN: RDRL-VTV Aberdeen Proving Ground, MD 21005-5066				8. PERFORMING ORGANIZATION REPORT NUMBER ARL-TR-7598	
9. SPONSORING/MONITORING AGENCY NAME(S) AND ADDRESS(ES)				10. SPONSOR/MONITOR'S ACRONYM(S)	
				11. SPONSOR/MONITOR'S REPORT NUMBER(S)	
12. DISTRIBUTION/AVAILABILITY STATEMENT Approved for public release; distribution is unlimited.					
13. SUPPLEMENTARY NOTES					
14. ABSTRACT Thermoacoustic excitation from carbon nanotube thin films was explored as a potential aerodynamic flow control approach. More broadly, the fundamental physics of the proposed direct turbulence dissipation scale (i.e., Kolmogorov scale) forcing was studied. Initial attempts to force a turbulent shear layer in the Kolmogorov scale did not exhibit noticeable differences from the baseline unforced system. Based on theoretical derivations, we hypothesized that the lack of coupling between the organized wave and the turbulence was due to low initial turbulent kinetic energy and low forcing amplitude. A new turbulent jet was designed and characterized with an order of magnitude higher turbulent kinetic energy. This system will be forced with high-amplitude piezoelectric transducers in future work to finalize the study of Kolmogorov scale forcing first proposed in the Director's Research Initiative.					
15. SUBJECT TERMS aerodynamic flow control, turbulence, fluid mechanics, nonlinear coupling, planar jet experiment, Director's Research Initiative (DRI)					
16. SECURITY CLASSIFICATION OF:			17. LIMITATION OF ABSTRACT UU	18. NUMBER OF PAGES 34	19a. NAME OF RESPONSIBLE PERSON Bryan Glaz
a. REPORT Unclassified	b. ABSTRACT Unclassified	c. THIS PAGE Unclassified			19b. TELEPHONE NUMBER (include area code) 410-278-2421

Contents

List of Figures	iv
List of Tables	iv
Acknowledgments	v
1. Introduction	1
2. Turbulent Jet System	3
3. Theory: Turbulent and Organized Fluctuation Coupling	5
4. Theory: Turbulent Kinetic Energy Spectrum	7
5. Results	11
5.1 Theoretical Results	11
5.2 Baseline Turbulent Jet	16
5.3 Forced Turbulent Jet	22
6. Conclusions	23
7. References	24
Distribution List	26

List of Figures

Fig. 1	Diagram of turbulent jet setup	4
Fig. 2	Plot of the unforced energy-spectrum function versus wavenumber...	12
Fig. 3	Forced energy-spectrum function with variable amplitude	13
Fig. 4	Energy-spectrum function with forcing in the inertial, transition, and dissipative subranges	14
Fig. 5	Energy-spectrum function with variable ratio of forced to unforced energy dissipation rate	15
Fig. 6	Energy-spectrum function with cumulative effect of forcing function and enhanced energy dissipation rate	15
Fig. 7	Streamwise mean velocity contour	17
Fig. 8	Streamwise root mean square (RMS) velocity fluctuation contour.....	17
Fig. 9	Energy dissipation rate contour	18
Fig. 10	Spanwise variation in mean velocity at $x/\delta = 0.25$	19
Fig. 11	Spanwise variation in velocity fluctuation at $x/\delta = 0.25$	19
Fig. 12	Spanwise variation in Kolmogorov scale structure size at $x/\delta = 0.25$	20
Fig. 13	Spanwise variation in Kolmogorov scale passage frequency at $x/\delta = 0.25$	21
Fig. 14	Velocity power spectra versus frequency for $x/\delta = 0.25$, $y/\delta = 0$	22
Fig. 15	Measured sound pressure output 5 cm from a carbon nanotube (CNT) thin-film source at various frequencies; RMS power input was maintained at 12 W for each frequency	22

List of Tables

Table.	Forcing function parameters	13
--------	-----------------------------------	----

Acknowledgments

We are grateful to Dr Jeremy Gaston of the US Army Research Laboratory's (ARL's) Human Research and Engineering Directorate and Prof YuHuang Wang's research group at the University of Maryland for assistance with initial acoustic measurements and Dr Shashi Karna of ARL's Weapons and Materials Research Directorate for a very fruitful collaboration on fabricating and applying the carbon nanotube thin films. The initial turbulent jet experiments were conducted by Dr Matthew Munson (ARL/Army Research Office) during his time at ARL/Vehicle Technology Directorate (VTD). We acknowledge the hard work of Mr Tim Kreutzfeldt, University of Maryland graduate student, who has now carried on Matthew's work and is conducting follow-on turbulent jet experiments in conjunction with ARL as part of his master's thesis. The assistance and guidance of Dr John Hrynuk (ARL/VTD) and Mr Chris Kroninger (ARL/VTD) in conducting the turbulent jet experiments at ARL are gratefully appreciated.

INTENTIONALLY LEFT BLANK.

1. Introduction

Control of boundary layer aerodynamic flows holds the potential for enabling future aerodynamic platforms with performance beyond current capabilities. Adverse flow phenomena can lead to decreased lift/thrust, while increasing penalties such as drag and noise. Flow separation from an aerodynamic surface is one such adverse phenomenon. The onset of separation is a major inhibitor of aerodynamic performance for a variety of platforms such as rotorcraft, turbomachinery and engines, fuselages, and projectiles. Successful development of active aerodynamic flow control technologies that delay or prevent separation could lead to substantial performance improvements, including increased speed, maneuverability, payload capacity, and/or range. However, instances in which active flow control technologies have successfully transitioned from the laboratory onto fielded vehicles are extremely rare due to excessive weight penalties, high power consumption, limited internal volume available in air vehicles, increased mechanical complexity, and potentially catastrophic failure modes. Such difficulties are a testament to the challenges associated with development of new active flow control approaches given that separation control has received substantial attention from researchers for more than a century (Greenblatt and Wygnanski 2000).

Active flow control methods to modify turbulent flows have been in development for many decades. Active flow control methods typically rely on the periodic addition of energy or momentum into a system to alter the fluid transport. Potential aeronautics applications typically involve delaying the onset of boundary layer separation, inducing the reattachment of a separated boundary layer, or affecting drag transition. Periodic methods generally require less energy input than flow control methods that use continuous suction or blowing along a surface to maintain attachment (Greenblatt and Wygnanski 2000). However, even for periodic actuation approaches, weight, size, and power constraints have limited the usefulness of flow control to laboratory settings. While many new active flow control methods have since been developed, real world applications of these methods remain relatively scarce (Joslin and Miller 2009).

A popular active flow control method involves triggering an instability in the flow that creates turbulence and entrains slower fluid into the boundary layer (Greenblatt and Wygnanski 2000). An example of this is demonstrated by the experiments of Oster et al. (1978), wherein the periodic excitation of a turbulent flow induces Kelvin-Helmholtz instabilities that increase the rate of spread of the boundary layer. This form of active flow control has been well studied for excitation frequencies

less than 1,000 kHz (Greenblatt and Wygnanski 2000). One of the earliest active flow control experiments for separation control used loudspeakers to generate acoustic excitation, which was found to increase the lift coefficient and decrease the drag coefficient over an airfoil for an optimum frequency (Ahuja et al. 1983). As is typical with most acoustic actuation studies, the frequency of actuation was tuned to trigger shear layer instability. Furthermore, the acoustic forcing studies have used conventional loudspeakers, which are too large and heavy for integration into realistic manned air vehicles. The size and weight constraints become even more restrictive when considering unmanned microscale vehicles.

Theoretical examinations of turbulent statistics demonstrate that in addition to flow instabilities that can be described by linearized stability methods, excitation can also impact the flow through nonlinear interactions. Manipulation of the Navier-Stokes equations shows that the addition of excitation to a turbulent flow creates a nonlinear closure term resulting from the effect of the coherent applied wave disturbance on the background turbulent Reynolds stresses. This closure term has a nonnegligible effect on bulk flow energy and momentum transport and results in modified Orr-Sommerfeld differential equations governing linearized stability of the Navier-Stokes equations (Reynolds and Hussain 1972b). Theoretical analysis also suggests that the nonlinear contributions of excitation are inherently linked to the rates of turbulent decay and dissipation as the flow develops downstream (Liu 1971). A further theoretical study of nonlinear effects on the turbulent energy considerations suggest a direct relationship between amplitude of excitation and the spread rate of the shear layer, which is supported by experimental data (Chan 1974). These results imply that it is possible to directly interact with turbulent energy through excitation. However, although theoretical derivations of the nonlinear interactions of turbulent statistics suggest that the effects of excitation can be observed over a large range of excitation frequencies, experimental results have been limited to low-frequency excitation corresponding to flow instabilities. Therefore, the physics of forcing turbulent flows, including the effects on shear layer stability characteristics, through the nonlinear interaction mechanism when the actuation frequency is not near an instability mode are relatively unexplored.

One reason for limited study of flow control at high frequencies compared to Kelvin-Helmholtz-type modal frequencies is that actuators designed for high frequencies are limited. The emergence of modern piezoelectric actuators in flow control enabled excitation frequencies well beyond typical instability receptivity values and into the inertial subrange of turbulent kinetic energy (Wiltse and Glezer 1993). Using piezoelectric actuators Wiltse and Glezer explored dissipative subrange forcing frequencies that were an order of magnitude less than the passage frequency of the smallest turbulent eddies. Excitation in the dissipative subrange

demonstrated “enhanced energy transfer from the large to the small scales” and “a substantial increase in the dissipation and in the decay rate of turbulent kinetic energy” (Wiltse and Glezer 1998). This result provides compelling evidence that the coupling between kinetic energy scales can act as a mechanism for affecting turbulent flows when forcing beyond instability frequencies. However, piezoelectric devices tend to be resonance based and could face challenges in pushing into Kolmogorov scale frequencies for realistic systems that may not correspond well with piezoelectric actuator design frequencies. Furthermore, direct Kolmogorov scale forcing has yet to be explored.

Clearly, it would be desirable to develop a flow control approach that overcomes system integration barriers such as weight, volume, power consumption, and mechanical complexity. For example, if the flow excitation capability originated from the material properties of the wing or blade surface skin, then additional components and subsystems that take up internal volume would not be required. In this Director’s Research Initiative (DRI), we proposed to develop such an approach using carbon nanostructure-based thermoacoustic thin films (Xiao et al. 2008) that are integrated with the platform. This would be a fundamental departure from the convention that flow control actuators “must be intrusive” devices (Cattafesta and Sheplak 2011). To develop this approach, the DRI was focused on understanding the fundamental and unexplored physics of Kolmogorov scale forcing on turbulent shear layers. Therefore, the primary hypothesis put forward in this work was that high-frequency forcing could alter the development of turbulent structures via nonlinear interaction mechanics that differ from the conventional instability-based flow control approaches.

2. Turbulent Jet System

To understand the fundamental fluid dynamics associated with high-frequency forcing, a canonical turbulent jet experiment was designed. Our study centers on previously unexplored regimes of fluid dynamics related to direct interaction with turbulence kinetic energy scales approaching those at which turbulent eddies are dissipated by viscous forces. To the best of our knowledge, no other studies have explore this regime of flow physics. To evaluate forced turbulent flow with an excitation frequency near the Kolmogorov scale, initial unforced turbulent flow data are needed to serve as a comparison.

A diagram of the setup of the turbulent jet used in the baseline characterization experiment is shown in Fig. 1. All parts were 3-D printed from a Fortus 400mc using the thermoplastic ABSM30. The upstream end of the jet consists of an inlet fitted for a compressed air hose followed by an initial section containing a grid

mesh structure that acts as a flow straightener. The downstream end of the jet has a contraction region that connects to the jet conduit with a contraction ratio of 25. The conduit is 50.8 cm long and 2.54 cm wide. Flow inside of the conduit is assumed to behave like flow inside of a square duct, which requires a longer distance to become fully developed than unbounded flow (Melling and Whitelaw 1976). The length of the conduit was chosen such that the flow is nearly fully turbulent at the jet exit for a Reynolds number of 11,000.

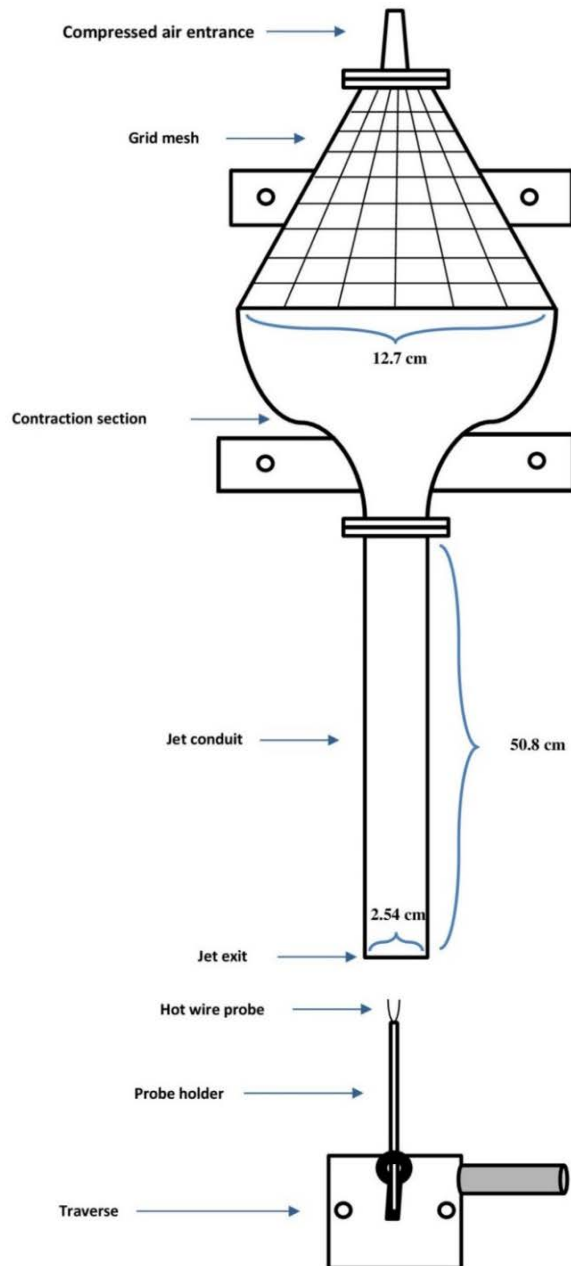


Fig. 1 Diagram of turbulent jet setup

All measurements were taken using a Dantec MiniCTA hot-wire anemometer system that uses a 1-dimensional (1-D) single sensor wire. The probe is held in place by a vertical mount positioned downstream such that the probe is positioned at the center of the jet exit on the vertical axis. The mount is screwed onto a 1-D traverse that can precisely alter the spanwise position of the probe. The streamwise position of the probe is fixed for each collection of spanwise measurements and repositioned using markings on the probe holder.

The hot-wire probe measures the streamwise velocity at 10 downstream locations between $0.25 \leq x/\delta \leq 2.50$ and $0 \leq y/\delta \leq 1.00$, where δ is the diameter of the jet exit. Velocity measurements are taken for 10 s at each location to obtain mean velocity and root mean square velocity fluctuation measurements. The energy dissipation rate ε is approximated using Taylor's hypothesis:

$$\varepsilon = 15\nu \frac{1}{U_1^2} \overline{\left(\frac{\partial u'_1}{\partial t} \right)^2}, \quad (1)$$

where ν is the kinematic viscosity of air, U_1 is the mean streamwise velocity and u'_1 is the root mean square fluctuating velocity in the streamwise direction. The Kolmogorov scale of turbulent structures is calculated from the energy dissipation rate estimated in Eq. 1 and the kinematic viscosity of air, which is assumed to be $1.69 \cdot 10^{-5}$ Pa·s in the laboratory.

$$\eta = (\nu^3 / \varepsilon)^{1/4}. \quad (2)$$

The passage frequency for the Kolmogorov scales structures is defined by

$$f_\eta = 0.5U_0 / \eta. \quad (3)$$

3. Theory: Turbulent and Organized Fluctuation Coupling

In addition to the experimental component of the DRI, complementary theoretical derivations were undertaken to help understand the basic flow physics and the dominant coupling terms between the fluctuation and turbulence kinetic energy. For the turbulent jet mean flow and kinetic energy transport, plane jet assumptions were employed (Rajaratnam 1976). Following the decomposition proposed by Reynolds and Hussain (1972a, 1972b), the velocity state is decomposed into a time-averaged component $\langle u \rangle$, turbulent fluctuations $u'(t)$, and an applied organized wave (periodic) component $\tilde{u}(t)$. Thus, the total streamwise velocity is

$$u(t) = \langle u \rangle + \tilde{u}(t) + u'(t). \quad (4)$$

In addition, from Reynolds and Hussain (1972a, 1972b),

$$\langle \tilde{u} \rangle = \langle u' \rangle = 0 \quad ; \quad \langle \langle u(t) \rangle \rangle = \langle u \rangle + \tilde{u}(t), \quad (5)$$

where $\langle \langle u \rangle \rangle$ is the phase-averaged velocity.

Using Eqs. 4 and 5, the mean flow kinetic energy is

$$\frac{1}{2} \frac{d}{dx} \int \langle u \rangle^3 dy = - \int \langle -\tilde{u}\tilde{v} \rangle \frac{\partial \langle u \rangle}{\partial y} dy - \nu_t \int \left(\frac{\partial \langle u \rangle}{\partial y} \right)^2 dy, \quad (6)$$

where the Boussinesq assumption for turbulent shear stress as applied to the plane jet has been invoked; for example,

$$\langle -u'v' \rangle = \nu_t \frac{\partial \langle u \rangle}{\partial y}. \quad (7)$$

To obtain the organized fluctuation kinetic energy, the time-averaged momentum is subtracted from the phase-averaged momentum equation. However, this leads to the Reynolds-Hussain organized disturbance closure term,

$$r_{12} = \langle \langle u'v' \rangle \rangle - \langle u'v' \rangle. \quad (8)$$

If Eq. 8 is interpreted to be the oscillation of the Reynolds stresses due to the applied organized fluctuation, then we can assume a Newtonian shear stress model

$$r_{12} = \langle \langle u'v' \rangle \rangle - \langle u'v' \rangle = \nu_t \left(\frac{\partial \tilde{u}}{\partial y} + \frac{\partial \tilde{v}}{\partial x} \right). \quad (9)$$

This leads to the fluctuation kinetic energy balance equation

$$\frac{1}{2} \frac{d}{dx} \int \left(\langle \tilde{u}^2 \rangle + \langle \tilde{v}^2 \rangle \right) \langle u \rangle dy = + \int \langle -\tilde{u}\tilde{v} \rangle \frac{\partial \langle u \rangle}{\partial y} dy - \nu_t \int \left[\left\langle \left(\frac{\partial \tilde{u}}{\partial y} \right)^2 \right\rangle + \left\langle \left(\frac{\partial \tilde{v}}{\partial y} \right)^2 \right\rangle + \left\langle \left(\frac{\partial \tilde{u}}{\partial x} \right)^2 \right\rangle + \left\langle \left(\frac{\partial \tilde{v}}{\partial x} \right)^2 \right\rangle \right] dy. \quad (10)$$

From a dimensional analysis argument, the eddy viscosity is proportional to the square of the turbulent kinetic energy divided by turbulence dissipation rate,

$$\nu_t \propto \frac{k_0^2}{\varepsilon_0}. \quad (11)$$

If the applied forcing is harmonic, then

$$\tilde{u} = A\varphi(y)e^{i(kx-\omega t)} + c.c. \quad (12)$$

where A is the amplitude, φ is a shape function. This leads to

$$\int \left[\left\langle \left(\frac{\partial \tilde{u}}{\partial y} \right)^2 \right\rangle + \left\langle \left(\frac{\partial \tilde{v}}{\partial y} \right)^2 \right\rangle + \left\langle \left(\frac{\partial \tilde{u}}{\partial x} \right)^2 \right\rangle + \left\langle \left(\frac{\partial \tilde{v}}{\partial x} \right)^2 \right\rangle \right] dy \propto A^2 . \quad (13)$$

Therefore, the nonlinear coupling between the turbulent fluctuations and the organized fluctuations are

$$\nu_t \int \left[\left\langle \left(\frac{\partial \tilde{u}}{\partial y} \right)^2 \right\rangle + \left\langle \left(\frac{\partial \tilde{v}}{\partial y} \right)^2 \right\rangle + \left\langle \left(\frac{\partial \tilde{u}}{\partial x} \right)^2 \right\rangle + \left\langle \left(\frac{\partial \tilde{v}}{\partial x} \right)^2 \right\rangle \right] dy \propto \frac{k_0^2}{\varepsilon_0} A^2 . \quad (14)$$

Equation 14 shows that the applied forcing couples into the turbulent kinetic energy according to the square of the amplitude.

4. Theory: Turbulent Kinetic Energy Spectrum

For the purposes of looking at spectral energy transfer, it is useful to examine the energy-spectrum function $E(k, t)$, which is a function of the wavenumber k and time t . Wavenumber k is defined as $2\pi/l$ where l is the size of the eddy. It is related to the passage frequency f by

$$k = \frac{\pi}{U_0 f} , \quad (15)$$

where U_0 is the mean velocity at the jet exit and passage frequency f is defined as $l/(2U_0)$.

The turbulent kinetic energy model derived in the subsequent sections is based on the Kolmogorov's hypothesis of local isotropy. This hypothesis requires that the turbulent statistics of a given eddy are on average invariant with respect to its location in the flow or rotation of the coordinate system. Large eddies are impacted by the mean flow and are thus statistically anisotropic, but as energy is passed to smaller scale eddies, this information is lost and at a sufficiently small scale, eddies become statistically isotropic. This characteristic of the energy cascade creates a subscale of wavenumbers at which the corresponding eddies have universal properties depending on the dissipation rate ε and the viscosity ν (Pope 2000). The assumption of local isotropy limits the application of the model to small scales that contain little energy.

The spectral energy of a turbulent flow can be quantified according to the energy balance equation:

$$\frac{\partial}{\partial t} E(k, t) = -\frac{\partial}{\partial k} T_K(k, t) - 2\nu k^2 E(k, t) + P_K(k, t) , \quad (16)$$

in which T_K is the net rate of energy transfer with respect to wavenumber, $2\nu k^2 E(k)$ represents the energy dissipation, and P_K is the production spectrum. As a result of the assumption of local isotropy, solutions for the energy-spectrum function typically set the energy production term to zero because large, energy-containing eddies are not considered. However, the following derivation hypothesizes that the addition of an excitation source within the range of isotropic turbulence makes the production term nonnegligible. Conservation of energy is also assumed to simplify Eq. 16, leading to

$$P_K(k) = \frac{\partial}{\partial k} T_K(k) + 2\nu k^2 E(k) . \quad (17)$$

The implication of this relation is that the effect of the excitation on the energy-spectrum function must be balanced by the net rate of energy transfer and the energy dissipation rate when the system is in equilibrium. Wiltse and Glezer (1998) found that excitation results “in enhanced energy transfer from the large to the small scales and in a substantial increase in the dissipation and in the decay rate of turbulent kinetic energy”. In the derivation that follows, the energy-spectrum function is derived both without and with the production term to model the unforced and forced spectra, respectively.

Models of T_K have been developed that allow Eq. 17 to be solved for $E(k)$ (Panchev 1971). However, few approximations assume a nonlocal model for which T_K depends on the energy at higher or lower wavenumbers. One theory that does make such an assumption is Heisenberg’s Spectral Theory. This theory proposes that T_K takes the form (Panchev 1971):

$$T_K(k) = \nu_T(k) \int_0^k 2E(k') k'^2 dk' , \quad (18)$$

in which ν_T is the turbulent eddy viscosity and is given by

$$\nu_T(k) = \frac{8}{9} \alpha^{-3/2} \int_k^\infty \sqrt{E(k')} k'^{-3/2} dk' , \quad (19)$$

in which α is an empirical constant corresponding to the inertial range of the energy-spectrum function. Equation 17 is rewritten in integral form with the assumption that P_K is zero without excitation:

$$\varepsilon_0 = T_K(k) + 2\nu \int_0^k E(k') k'^2 dk' . \quad (20)$$

The dissipation rate is represented by ε_0 and is assumed constant. Equations 18–20 can be combined to obtain

$$\varepsilon_0 = \frac{8}{9} \alpha^{-3/2} \int_k^\infty \sqrt{E(k')} k'^{-3/2} dk' \int_0^k 2E(k') k'^2 dk' + 2\nu \int_0^k E(k') k'^2 dk' . \quad (21)$$

To simplify Eq. 20, the dimensionless variables x and $\Psi(x)$ are substituted:

$$x = \alpha^{3/4} (\nu^3 / \varepsilon_0)^{1/4} k , \quad (22)$$

$$\Psi(x) = \alpha^{-9/4} (\varepsilon_0 \nu^5)^{-1/4} E(x) , \quad (23)$$

which transforms Eq. 21 into

$$1 = \left(1 + \frac{8}{9} \int_x^\infty \sqrt{\Psi(x')} x'^{-3/2} dx' \right) \int_0^x 2\Psi(x') x'^2 dx' . \quad (24)$$

By substituting in the dissipation function,

$$D(x) = \int_0^x 2\Psi(x') x'^2 dx' , \quad (25)$$

where

$$D(\infty) = 1 , \quad (26)$$

$$\Psi(x) = \frac{1}{2x^2} \frac{dD}{dx} , \quad (27)$$

leads to

$$1 = \left(1 + \frac{8}{9\sqrt{2}} \int_x^\infty \sqrt{\frac{dD}{dx'}} x'^{-5/2} dx' \right) D(x) . \quad (28)$$

This equation can be used to find a differential equation for $D(x)$.

$$\frac{dD}{dx} = \frac{32}{81} D(x)^4 x^{-5} . \quad (29)$$

The solution to this differential equation is

$$D(x) = \left(1 + \frac{8}{27} x^{-4} \right)^{-3} , \quad (30)$$

which corresponds to the following solution for $\Psi(x)$ (Panchev 1971):

$$\Psi(x) = \frac{16}{81} \frac{x^{-7}}{\left(1 + \frac{8}{27} x^{-4} \right)^{4/3}} . \quad (31)$$

To account for changes in the energy-spectrum function due to the addition of periodic forcing, the energy balance equation must be adapted to introduce a forcing function. The following method introduces forcing in the form of a production term. As shown in Eq. 16, production is generally assumed to be zero in the range of isotropic turbulence. However, when forcing is introduced in the wavenumber range of isotropic turbulence, this assumption is no longer valid for the forced energy balance equation. Wiltse and Glezer (1998) note that excitation adds energy to the flow, so the following theoretical model is assumed to take place when the flow has reached equilibrium.

After reintroducing the production term, Eq. 20 becomes

$$\varepsilon = T_K(k) + 2\nu \int_0^k E(k') k'^2 dk' - \int_0^k P_K(k') dk' . \quad (32)$$

Wiltse and Glezer (1998) show that external excitation forces the turbulent fluctuating velocity u' to oscillate at a given frequency in the time domain. Turbulent kinetic energy is proportional to u'^2 , leading to the following approximate production term in the time domain:

$$P_K(t) \sim \sin^2(\omega t) = \sin(2\omega t) , \quad (33)$$

where ω is the forcing frequency. A Fourier transform of this result moves P_K into the frequency domain, which is then converted to wavenumber using Eq. 1.

$$P_K(k) \sim (\delta(k - 2k_f)) , \quad (34)$$

The delta function $\delta(k - 2k_f)$ indicates an impulse at twice the forcing wavenumber k_f . For the purposes of using the production term in a numerical ODE (ordinary differential equation) solver, the production term cannot be discontinuous. Thus, a Gaussian function is chosen to replace the impulse.

$$P_K(k) = A e^{-(k-2k_f)^2 / 2a^2} , \quad (35)$$

where A and a are the amplitude and width of the Gaussian function, respectively. For consistency with the solution for the unforced energy-spectrum function, the production term is also replaced with dimensionless variables such that

$$P(x) = A e^{-(x-b)^2 / (2a^2)} . \quad (36)$$

The amplitude A has been absorbed from Eq. 35, and b represents twice the forcing wavenumber as a function of the dimensionless wavenumber x . Accordingly, Eq. 23 can be rewritten as

$$1 = \left(1 + \frac{8}{9} \int_x^\infty \sqrt{\Psi(x')} x'^{-3/2} dx' \right) \int_0^x 2\Psi(x') x'^2 dx' - \int_0^x P(x') dx'. \quad (37)$$

Wiltse and Glezer (1998) found that the energy dissipation rate in the forced flow was twice as high as the dissipation rate in the unforced flow on the jet centerline and more than 20 times larger than the dissipation rate in the unforced flow in the shear layer. Thus far, no assumption has been made on the value of ε_0 as it is embedded into the dimensionless variables x and Ψ in Eqs. 22 and 23 and also the boundary condition for the dissipation spectrum in Eq. 13. The effect of the ratio between the forced energy dissipation rate ε_f and the unforced energy dissipation rate ε_0 will be examined more thoroughly in the Section 5. The same steps followed in the unforced energy-spectrum function derivation are followed to obtain a differential equation for $D(x)$.

$$\frac{dD}{dx} = \frac{\frac{8}{9\sqrt{2}} \sqrt{\frac{dD}{dx}} D(x)^2 x^{-5/2} + D(x)P(x)}{1 + \int_0^x P(x') dx'}. \quad (38)$$

This differential equation cannot be separated to find an analytical solution to $D(x)$ as was done in Eq. 31. However, using the boundary condition from Eq. 26, a numerical solution can be obtained to approximate the form of $\Psi(x)$.

5. Results

5.1 Theoretical Results

For consistency, all plots for the energy-spectrum function were obtained using the dimensionless variables derived Eqs. 21 and 22.

For the unforced spectrum, there is an exact solution to the differential equation for the energy-spectrum function as shown in Eq. 38. This solution is shown in Fig. 2.

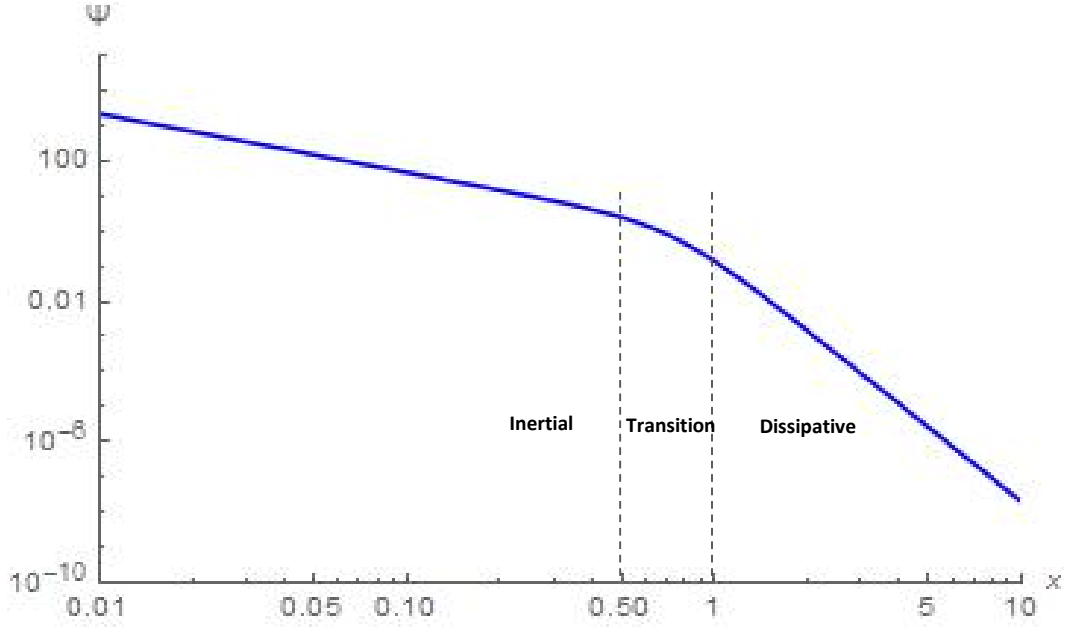


Fig. 2 Plot of the unforced energy-spectrum function versus wavenumber

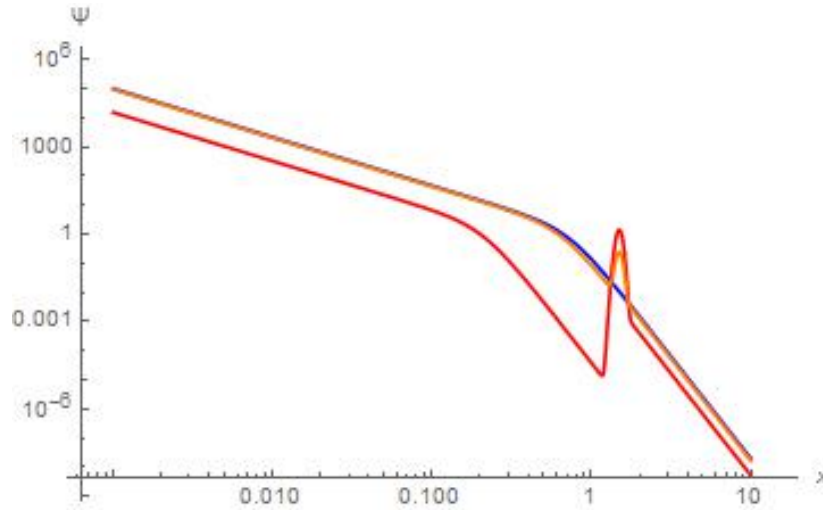
There are 3 distinct regions on the plot of the unforced energy-spectrum function. At small x the slope of the curve follows $x^{-5/3}$, which is indicative of the inertial subrange of the energy spectrum. Around $x = 0.5$ there is a transition region where the slope decreases until balancing out at about $x = 1$. For large x the slope of the curve follows x^{-7} , indicating the beginning of the dissipative subrange of the energy spectrum. The transition of the slope from the inertial subrange to dissipative range is abrupt and does a poor job of resembling experimental data relative to local models for T_K (Panchev 1971).

For the forced spectrum, solutions were obtained in Wolfram Mathematica by numerically solving the differential equation in Eq. 38 using the boundary condition in Eq. 25. Experimentally, the amplitude A and wavenumber b of the excitation are the main parameters of interest. In addition, the ratio of ε_f to ε_0 was varied to examine the effect of the enhanced energy dissipation rate in forced flow. The solution does not converge for very small values of a or very large values of A , and the respective minimum and maximum to maintain convergence varied depending on the chosen value of b . The parameters for the chosen forcing function $P(x)$ from Eq. 36 and the energy dissipation rate ratios are shown in the following Table. The effects of the given parameters on the energy-spectrum function are examined in Figs. 3–6. In each of these plots of the forced energy-spectrum function, the unforced spectrum is shown in blue for reference.

Table. Forcing function parameters

Figure	b	A	a	$\varepsilon t/\varepsilon_0$
3 (orange)	1.5	1.0	0.06	1
3 (red)	1.5	12.5	0.06	1
4 (orange)	0.5	3.5	0.20	1
4 (green)	1.0	3.5	0.20	1
4 (red)	5.0	3.5	0.20	1
5 (orange)	2
5 (red)	20
6 (orange)	2.0	5.0	0.10	2
6 (red)	2.0	5.0	0.10	20

Figures 3 and 4 show the behavior of the forced energy-spectrum function as a result of varying individual parameters of $P(x)$. An interesting result of the forced energy-spectrum functions is their behavior at wavenumbers before the spike. The introduction of the forcing function to the differential equation in Eq. 38 appears to reduce the amount of energy at the beginning the spectrum when the amplitude is nonzero. As shown in Fig. 3 increasing this amplitude results in a greater reduction of energy at the beginning of the spectrum relative to the unforced energy-spectrum function. Also, the forcing function seems to cause a gradual decrease of energy leading up to the spike. Increasing the amplitude causes this gradual decrease to take place over a wider range of wavenumbers. The addition of the production term also results in an earlier onset of the dissipative range.

**Fig. 3 Forced energy-spectrum function with variable amplitude**

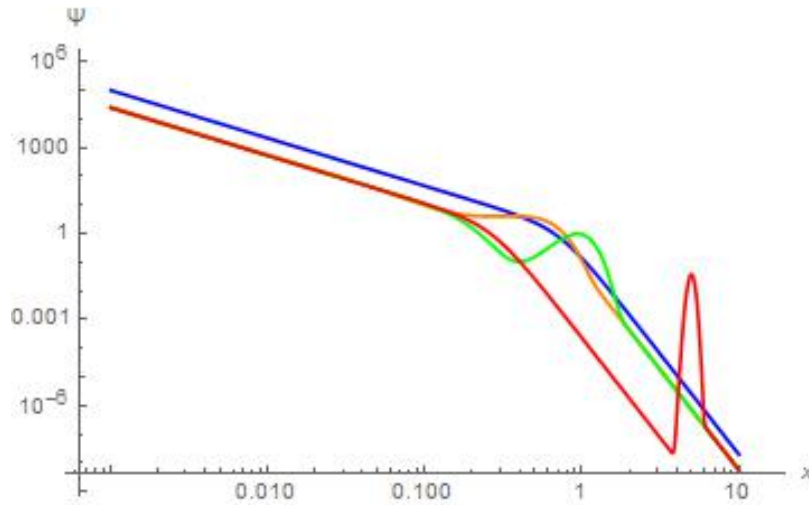


Fig. 4 Energy-spectrum function with forcing in the inertial, transition, and dissipative subranges

Figure 4 shows the energy-spectrum functions with the same amplitude and width forcing in the inertial, transition, and dissipative ranges. Unlike varying the amplitude, varying the forcing wavenumber has no effect on the amount of energy at the beginning of the spectrum. However, it appears to have a significant effect on the decrease in energy before the spike. The decline in energy before the spike with dissipative range forcing noticeably has a much wider range of wavenumbers than transition or inertial range forcing.

Figure 5 shows the effect of varying the ratio of the forced to unforced energy dissipation rate on the energy-spectrum function without introducing a production term. Experimental results suggest that excitation can increase the energy dissipation rate in a flow by up to a factor of 20 (Wiltse and Glezer 1998). Increasing the energy dissipation rate appears to increase the energy at all wavenumbers in the inertial and dissipative ranges. Furthermore, the onset of the dissipative range occurs at a larger wavenumber as the energy dissipation rate is increased. The energy dissipation rate appears to have an opposite effect of the production term. Relative to the unforced case, increasing the amplitude of the production term seems to decrease energy at all wavenumbers outside of the spike and cause an earlier onset of the dissipative range.

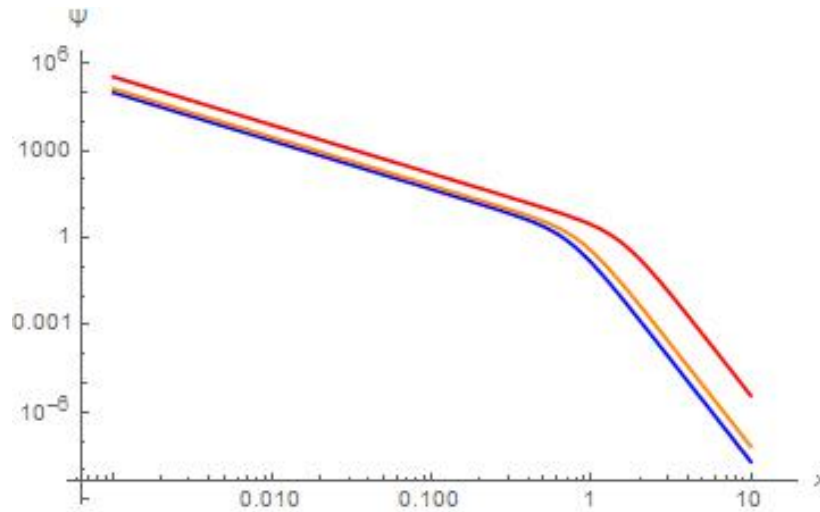


Fig. 5 Energy-spectrum function with variable ratio of forced to unforced energy dissipation rate

The opposing effects of the production term and the energy dissipation rate on the energy-spectrum function beg the question of which effect has a greater influence on the forced energy-spectrum function as a whole. Figure 6 shows that depending on the energy dissipation rate ratio, the forced energy-spectrum function can either contain more or less energy than the unforced spectrum. Wiltse and Glezer's (1998) experimental data show more energy in the forced case than the unforced case. It also shows that the transition into the dissipative range occurs at a larger wavenumber than the unforced case. Both of these observations indicate that the effect of the enhanced energy dissipation rate in the forced flow has a greater effect on the energy-spectrum function than the production term.

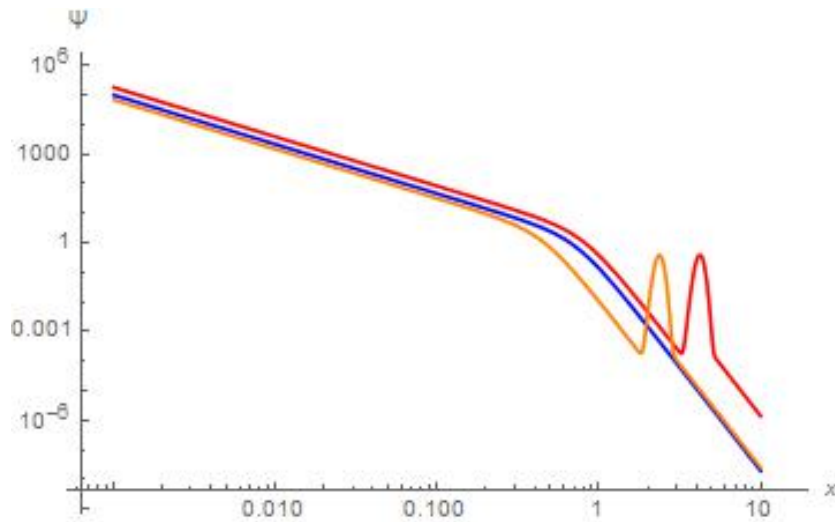


Fig. 6 Energy-spectrum function with cumulative effect of forcing function and enhanced energy dissipation rate

It should be noted that because Heisenberg's Spectral Theory deals only with isotropic turbulence past the energy-containing subrange of the energy-spectrum function, all of the theoretical results discussed previously cannot be extended to compare with experimental results in the range of large, anisotropic eddies. While theoretical results are useful in the inertial and dissipative subranges, the inherently anisotropic energy-containing subrange requires further analysis. Wiltse and Glezer's (1998) finding that there is a reduction in energy in the energy-containing range of wavenumbers when excitation is introduced is an important result that cannot be explained by isotropic turbulence models. Although these models can adequately explain the reasoning for the enhanced energy in the inertial and dissipative ranges, they give no insight into why the energy-containing range in the forced case contains less energy than the unforced case. The limits for convergence of a solution to the differential equation in Eq. 34 also necessitate further examination. Forcing functions with larger, narrower spikes would resemble experimental data more closely, so alternative methods to finding solutions should be considered.

5.2 Baseline Turbulent Jet

At the jet exit, the mean streamwise velocity U_0 is 6.75 m/s and the turbulent intensity is 4.36%. In the plots that follow, the spanwise centerline of the jet is represented by $y/\delta = 0$ and the walls of the jet exit are located at $x/\delta = 0$ and $y/\delta = \pm 0.5$. The closest spanwise location for which measurements are taken is $x/\delta = 0.25$. Contours of the mean velocity, velocity fluctuation, and energy dissipation rate are shown in Figs. 7–9. For visualization purposes, spanwise symmetry is assumed and the velocity data obtained for $0 \leq y/\delta \leq 1$ are reflected over the x/δ axis.

As shown in Fig. 7, the mean velocity is highest at the centerline of the jet. Close to the jet exit, the mean velocity is zero for $y/\delta > 0.50$. Farther downstream, the shear layer expands outward and the mean velocity is nonzero for $y/\delta > 0.50$.

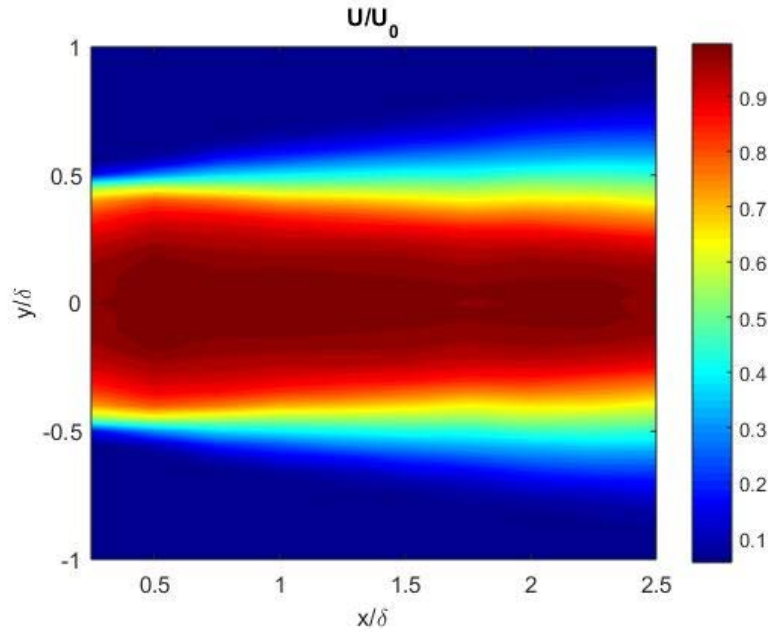


Fig. 7 Streamwise mean velocity contour

The velocity fluctuation in Fig. 8 provides a visual of the expansion of the shear layer as the flow moves downstream. The largest fluctuating velocity is located just before the boundary of the jet exit at $y/\delta = 0.50$. This region of large velocity fluctuation expands and follows the shear layer. At each axial location within the shear layer, the velocity fluctuation has a minimum at the centerline but gradually increases closer to the wall.

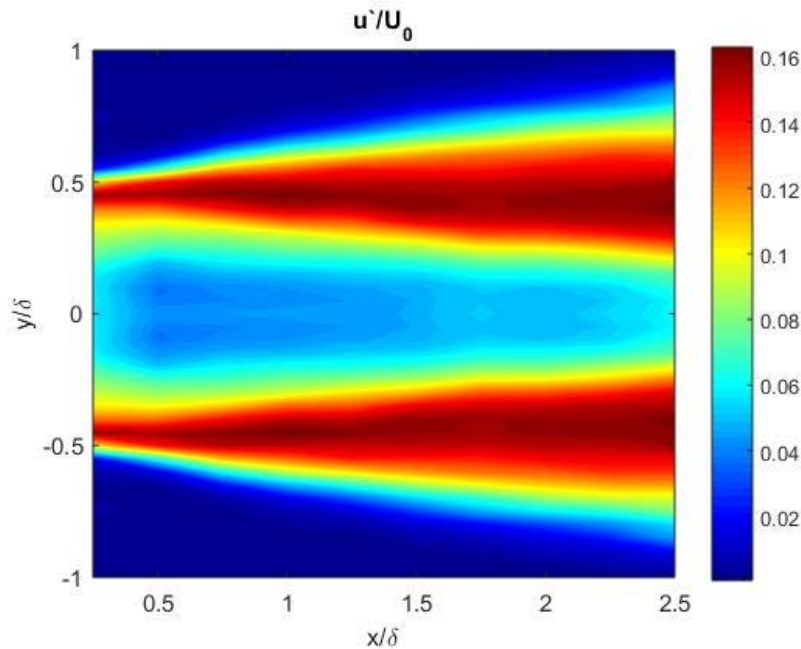


Fig. 8 Streamwise root mean square (RMS) velocity fluctuation contour

Similar to the velocity fluctuation, the energy dissipation rate shown in Fig. 9 is smallest at the jet centerline and increases as the spanwise location approaches $y/\delta = 0.50$. Unlike the velocity fluctuation, the region of large energy dissipation rate following the shear layer decreases downstream of the jet exit.

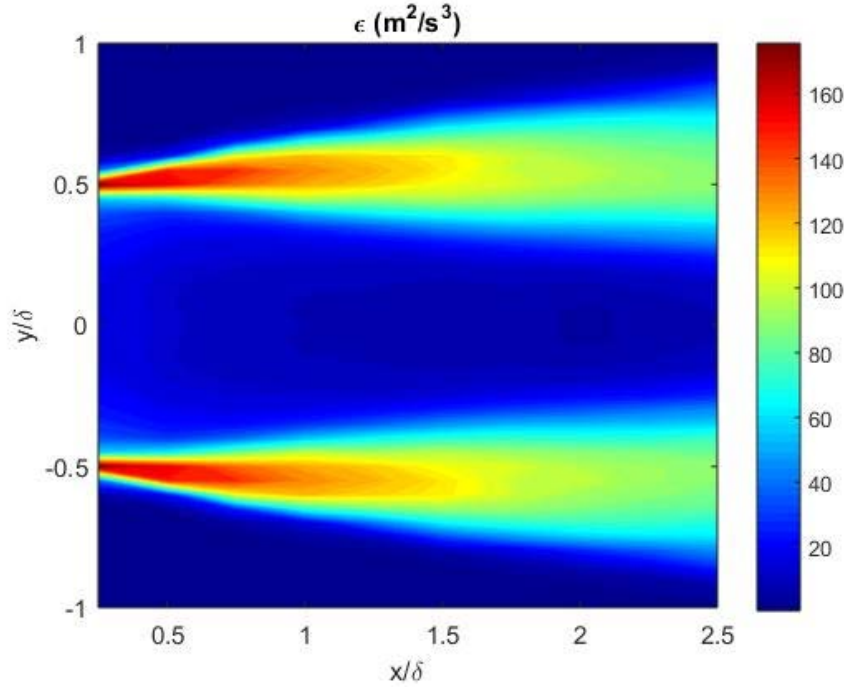


Fig. 9 Energy dissipation rate contour

The spanwise variations of the mean velocity and turbulent velocity fluctuation at $x/\delta = 0.25$ are shown in Figs. 10 and 11. Again, the data are reflected across the x/δ axis due to the assumption of symmetry. The gradual spanwise decrease in mean velocity from the maximum at $y/\delta = 0$ to near zero at $y/\delta = 0.50$ is typical of a turbulent jet in fully turbulent flow (Rajaratnam 1976). The mean velocity profile differs from the “top-hat” shape expected in the viscous core region of a turbulent jet (Dimitriadus et al. 2012), signifying that the chosen length of the jet conduit is sufficiently long for the flow to be fully turbulent at $x/\delta = 0.25$. The velocity fluctuation profile has sharp peaks near the edges of the shear layer and a relatively flat region near the jet centerline. This is also different from the profile of flow that is not fully developed in which the peaks are not as pronounced and there is a noticeable minimum at the jet centerline (Dimitriadus et al. 2012).

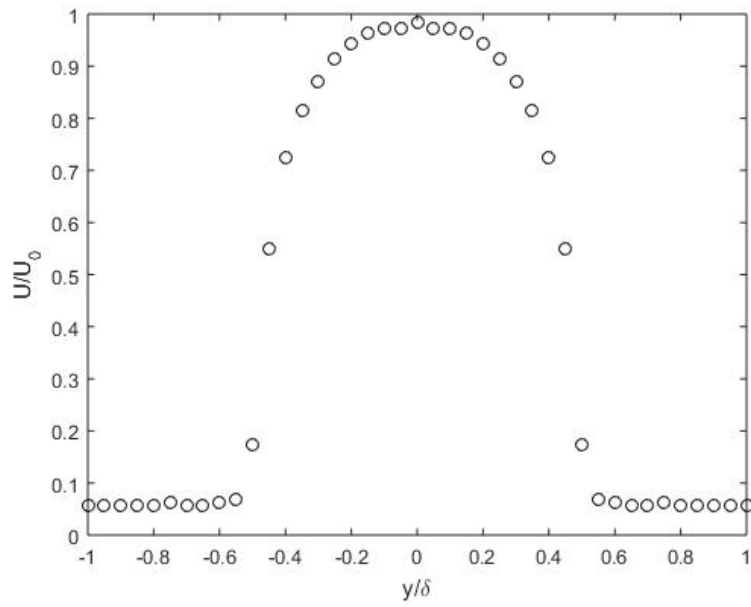


Fig. 10 Spanwise variation in mean velocity at $x/\delta = 0.25$

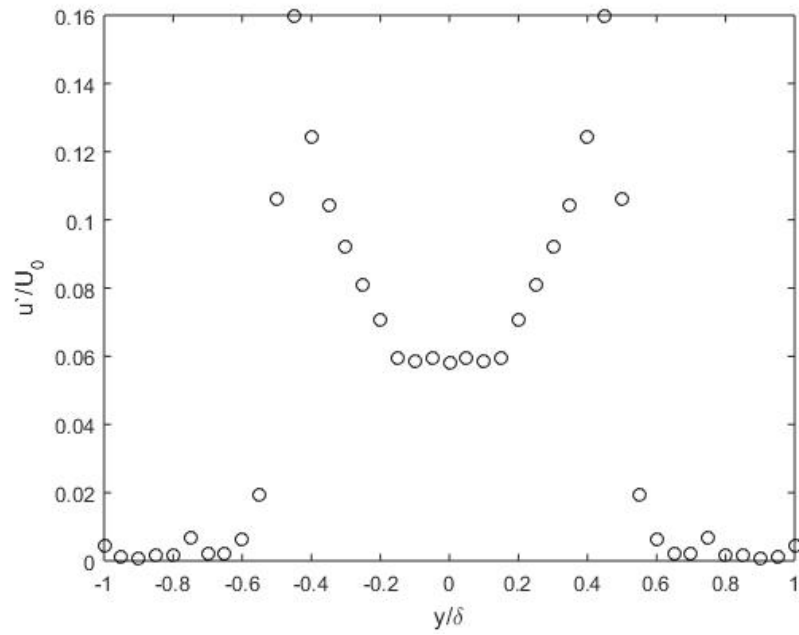


Fig. 11 Spanwise variation in velocity fluctuation at $x/\delta = 0.25$

The spanwise variation of the Kolmogorov scale (calculated from Eq. 31) at the closest downstream location is shown in Fig. 12. At $x/\delta = 0.25$, the maximum Kolmogorov scale structure size of 0.121 mm is located at the jet centerline. The minimum Kolmogorov structure size of 0.068 mm is located at $y/\delta = 0.50$. Planned experiments involve excitation at the jet exit, and the excitation frequency would need to match the passage frequency of the Kolmogorov scale eddies to add forcing at the far end of the dissipative subrange. The corresponding passage frequencies calculated from Eq. 32 are plotted in Fig. 13. At the jet centerline the Kolmogorov scale passage frequency is at a minimum of 27.79 kHz. The maximum Kolmogorov scale passage frequency at $y/\delta = 0.50$ is 49.73 kHz. As noted by Wiltse and Glezer (1998), excitation leads to enhanced dissipation, which in turn corresponds to smaller Kolmogorov scale eddies relative to the unforced case. This suggests that adding excitation at the passage frequency of the unforced Kolmogorov scale structures will lead to smaller Kolmogorov scales in the forced case.

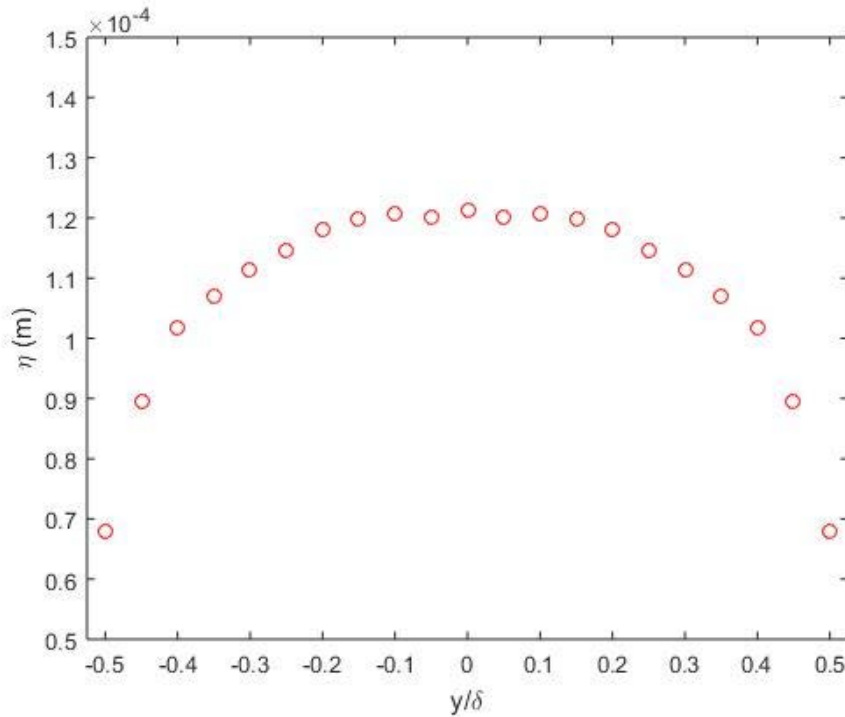


Fig. 12 Spanwise variation in Kolmogorov scale structure size at $x/\delta = 0.25$

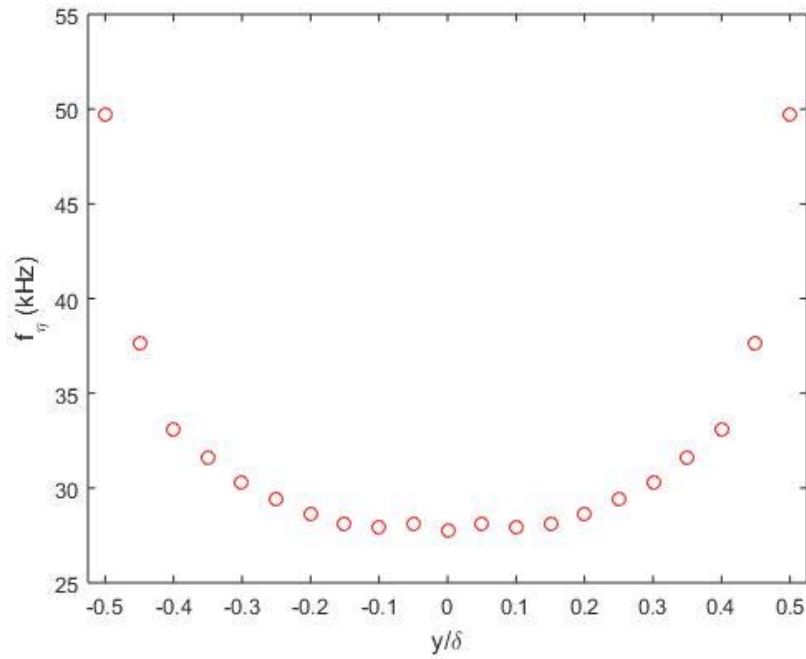


Fig. 13 Spanwise variation in Kolmogorov scale passage frequency at $x/\delta = 0.25$

Figure 14 shows the velocity power spectra of the flow at centerline for $x/\delta = 0.25$. Local smoothing was applied using binning of 10 neighboring points to reduce experimental noise. The response frequency of the hot-wire conditioner is 10 kHz, which results in a significant amount of noise in the data at the end of the spectrum shown in Fig. 15. As previously stated, the respective passage frequencies of the maximum and minimum Kolmogorov scale structures at $x/\delta = 0.25$ are 27.79 kHz and 49.73 kHz.

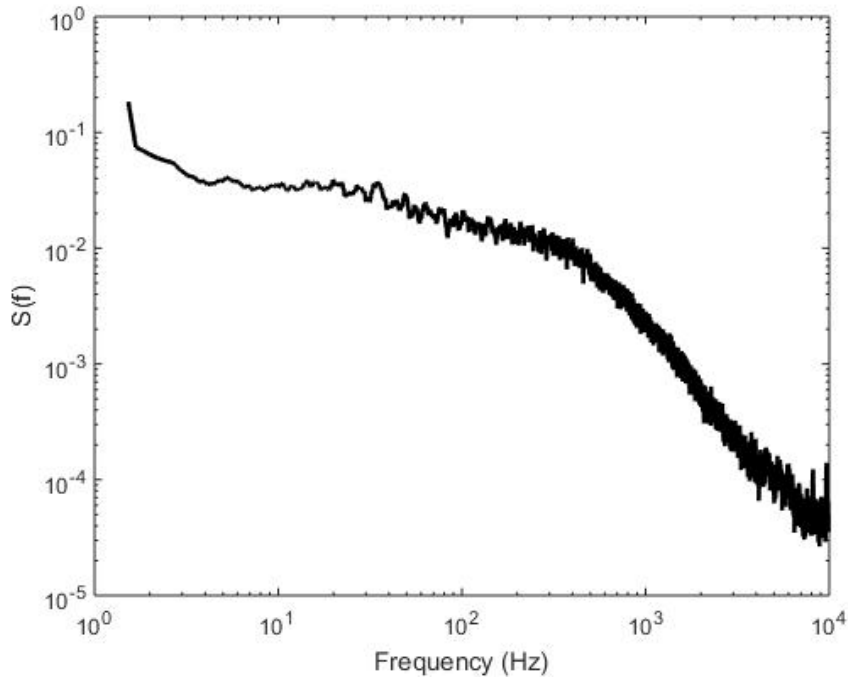


Fig. 14 Velocity power spectra versus frequency for $x/\delta = 0.25, y/\delta = 0$

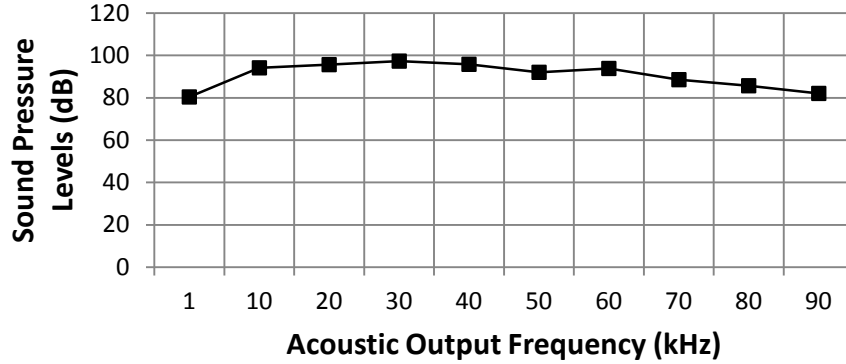


Fig. 15 Measured sound pressure output 5 cm from a carbon nanotube (CNT) thin-film source at various frequencies; RMS power input was maintained at 12 W for each frequency

5.3 Forced Turbulent Jet

Thermoacoustic emissions from CNT films were used to force the turbulent jet. Details of the CNT thin film and thermoacoustic characterization are summarized in Sun et al. (2016). A Kolmogorov passage frequency of 29 KHz was estimated for the turbulent jet conditions, which is easily within the performance capabilities of the thermoacoustic thin-film actuators. As shown in Fig. 15, it is clear that the

frequency response of the CNT acoustic output is fairly broadband at ultrasonic frequencies. In addition, a low baseline turbulence intensity of 0.21% was measured.

The turbulent jet was forced at 85 dB and 29 KHz. However, the forced turbulent kinetic energy spectrum did not show any measureable effect of the forcing. Based on Eq. 14, we hypothesize that the amplitude of the forcing was not sufficient and that the low turbulence intensity limited the nonlinear coupling. Although the fundamental objective of demonstrating Kolmogorov forcing effectiveness was not successful during the DRI period, higher-amplitude forcing studies are planned for follow-on mission research to finalize our study of basic physics due to Kolmogorov scale forcing. Furthermore, the new forced experiments will be conducted with the baseline jet with 4% turbulent intensity described in Section 5.2.

6. Conclusions

Our initial turbulent jet experiment conducted under the DRI—with very low turbulence intensity and low forcing amplitudes—showed no apparent coupling between the applied fluctuation and dissipative turbulent kinetic energy scales. However, the theoretical efforts of this DRI lead us to believe that the basic hypothesis of coupling with Kolmogorov scale forcing is not invalid. Rather, our current hypothesis is that the low forcing amplitudes and low turbulent kinetic energy intensity of the initial forced turbulent jet experiment limited the degree of coupling. As a result, follow-on experiments with higher forcing amplitudes and turbulent kinetic energy are underway as part of follow on mission research. Under this DRI, we have shown through theory that high-frequency forcing far away from instability scales can couple into the turbulence scales. In addition, we have shown how this coupling is expected to scale with various input parameters. From the nanomaterials perspective, novel approaches to augment the maximum possible power density that the CNT thin films can sustain were developed as part of joint ARL and University of Maryland research (Sun et al. 2016). These augmented thin films may be useful for high-power devices based on carbon nanomaterials.

7. References

- Ahuja KK, Whipkey RR, Jones GS. Control of turbulent boundary layer flows by sound. Proceedings of AIAA 8th Aeroacoustics Conference; 1983 Apr 11–13; Atlanta, GA; New York (NY): American Institute of Aeronautics and Astronautics (AIAA). AIAA Paper 83-0726.
- Cattafesta III LN, Sheplak M. Actuators for active flow control. Annual Review of Fluid Mechanics. 2011;43:247–272.
- Chan YY. Spatial waves in turbulent jets. Part II. Physics of Fluids. 1974;17(9):1667–1670.
- Dimitriadis P, Liveri-Dalaveri M, Kaldis A, Kotsalos C, Papacharalompous G, Papanicolaou P. Zone of flow establishment in turbulent jets. Proceedings of European Geosciences Union General Assembly 2012; 2012 Apr 22–29; Vienna, Austria. Athens (Greece): ITIA; 2012. Vol. 14, EGU2012-12716.
- Greenblatt D, Wygnanski I. The control of flow separation by periodic excitation. Progress in Aerospace Sciences. 2000;36(7):487–545.
- Joslin RD, Miller DN. Fundamentals and applications of modern flow control. Reston (VA): American Institute of Aeronautics and Astronautics; 2009.
- Liu JTC. Nonlinear development of an instability wave in a turbulent wake. Physics of Fluids. 1971;14(11):2251–2257.
- Melling A, Whitelaw JH. Turbulent flow in a rectangular duct. Journal of Fluid Mechanics. 1976;78(02):289–315.
- Oster D, Wygnanski I, Dziomba B, Fiedler H. On the effect of initial conditions on the two dimensional turbulent mixing layer. In: Fiedler H, editor. Structure and mechanisms of turbulence i: lecture notes in physics. Berlin (Germany): Springer Verlag; 1978. p. 48–64.
- Panchev S. Random functions and turbulence. Oxford (UK): Pergamon Press; 1971.
- Pope SB. Turbulent flows. Cambridge (UK): Cambridge University Press; 2000.
- Rajaratnam N. Turbulent Jets. Amsterdam (Netherlands): Elsevier Scientific Publishing; 1976.

- Reynolds WC, Hussain AKMF. The mechanics of an organized wave in turbulent shear flow. Part 2. Experimental results. *Journal of Fluid Mechanics*. 1972a;54(02):241–258.
- Reynolds WC, Hussain AKMF. The mechanics of an organized wave in turbulent shear flow. Part 3. Theoretical models and comparisons with experiments. *Journal of Fluid Mechanics*. 1972b;54(02):263–288.
- Sun C, Glaz B, Okada M, Baker E, Cheng X, Karna S, Wang Y. Blocking oxidation failures of carbon nanotubes through selective protection defects. *Nature Communications*. Under review. 2016.
- Wiltse J, Glezer A. Manipulation of free shear flows using piezoelectric actuators. *Journal of Fluid Mechanics*. 1993;249:261–85.
- Wiltse J, Glezer A. Direct excitation of small-scale motions in free shear flows. *Physics of Fluids*. 1998;10(8):2026–036.
- Xiao L, Chen Z, Feng C, Liu L, Bai Z-Q, Wang Y, Qian L, Zhang Y, Li Q, Jiang K, Fan S. Flexible, stretchable, transparent carbon nanotube thin film loudspeakers. *Nano Letters*. 2008;8(12):4539–4545.

1 DEFENSE TECHNICAL
(PDF) INFORMATION CTR
DTIC OCA

2 DIRECTOR
(PDF) US ARMY RESEARCH LAB
RDRL CIO LL
IMAL HRA MAIL & RECORDS
MGMT

1 GOVT PRINTG OFC
(PDF) A MALHOTRA

1 DIR USARL
(PDF) RDRL VTV
B GLAZ